Reduction of Backward Scatterings at the Low-Coherence Kunwu Laser Facility

Anle Lei,[1,*] Ning Kang ,[2,†] Yao Zhao,[3,‡] Huiya Liu,[2] Honghai An,[1] Jun Xiong,[1] Ruirong Wang,[1] Zhiyong Xie,[1] Yuchun Tu,[1] Guoxiao Xu,[2,5] Xichen Zhou,[1] Zhiheng Fang,[1] Wei Wang,[1] Lan Xia,[1] Wei Feng,[1] Xiaohui Zhao,[1] Lailin Ji,[1] Yong Cui,[1] Shenlei Zhou,[2] Zhanjun Liu,[4] Chunyang Zheng,[4] Lifeng Wang,[4] Yanqi Gao,[1] Xiuguang Huang,[1] and Sizu Fu[1]

[1]*Shanghai Institute of Laser Plasma, China Academy of Engineering Physics, Shanghai 201800, China*
[2]*Key Laboratory of High Power Laser and Physics, Shanghai Institute of Optics and Fine Mechanics,*
Chinese Academy of Sciences, Shanghai 201800, China
[3]*School of Science, Shenzhen Campus of Sun Yat-sen University, Shenzhen 518107, China*
[4]*Institute of Applied Physics and Computational Mathematics, Beijing 100094, China*
[5]*University of Chinese Academy of Sciences, Beijing 100049, China*

We report the first experimental observation on the reduction of backward scatterings by an instantaneous broadband laser with 0.6% bandwidth in conditions of interest for inertial confinement fusion at the low-coherence Kunwu laser facility. The backscatter of stimulated Brillouin scattering (SBS) was robustly reduced by half at intensities of 1–5×10^{14} W/cm^2 with the 0.53-μm broadband laser in comparison with the monochromatic laser. As SBS dominates energy loss of laser-plasma interactions, the reduction of that demonstrates the enhancement of laser-target coupling by the use of broadband laser. The mitigation of filamentation leads to the reduction of stimulated Raman backscattering at low intensities. In addition, the three-halves harmonic emission was reduced with the broadband laser as well.

Laser-plasma instabilities (LPI) are of great importance in direct-drive inertial confinement fusion (DDICF) [1–3], for its generation of scatterings and hot electrons causing energy loss and preheating. Apart from traditional beam smoothing methods, including phase plates [4], smoothing by spectral dispersion [5], and polarization smoothing [6], low-coherence laser technology [7–9] is a novel and promising way to solve the LPI problem. The theory basis for the low-coherence idea is simply that LPI will be naturally suppressed when its growth time is limited by the laser coherence time, which is usually achieved in theory and simulation by introducing a broadband pump laser [10,11]. The coherence time is decreased when the bandwidth increases, owing to the constant time-bandwidth product of laser pulse [12].

Generally speculating the potential capability of broadband laser on LPI suppression may not be difficult, but there are major obstacles to quantitatively obtaining the level of LPI reduction at a specific bandwidth. Efforts on several kinds of broadband laser models have been carried out, including random phase jump [13–16], frequency modulation [17], polychromatic light [9,18,19], and continuous broadband light [8,20,21]. Generally speaking, reduction of all main kinds of LPI concerned by the DDICF community using broadband laser have been reported, such as the stimulated Brillouin scattering (SBS) [22,23], the stimulated Raman scattering (SRS) [12,24–27], the two plasmon decay (TPD) [12,28], and

the cross-beam energy transfer (CBET) [29–32], but most of them are pure theoretical studies, which need experimental verification. In experiments, the difficulty is deploying broadband laser technology within the existing ICF optical framework, usually with a nearly monochromatic light source and highly bandwidth-sensitive frequency conversion processes. Therefore, conducting experiments directly under broadband laser conditions is a key step in developing and improving broadband LPI theory, as well as in future drive design.

In this Letter, we present the first experimental results regarding the effect of broadband laser on LPI including SBS, SRS, and TPD. The experiments were conducted at the Kunwu laser facility of Shanghai Institute of Laser Plasma [33]. Two sets of data were obtained in the experiments, respectively, with the broadband laser and the narrow band laser, in which the narrow band laser is the second harmonic of a conventional neodymium glass laser whose bandwidth is small enough to be roughly treated as monochromatic in LPI analyses. The broadband laser is produced by amplifying a superluminescent pulse in a neodymium glass amplifier, during which spectrum shaping techniques are used to compensate for the gain narrowing effect [34]. The fundamental wave (∼1.06 μm) has a bandwidth of ∼13 nm [7], and a 17% deuterium-doped deuterated potassium dihydrogen phosphate (DKDP) crystal is used to convert it to the second harmonic at ∼65% efficiency, resulting in an output green laser with ∼3.2-nm
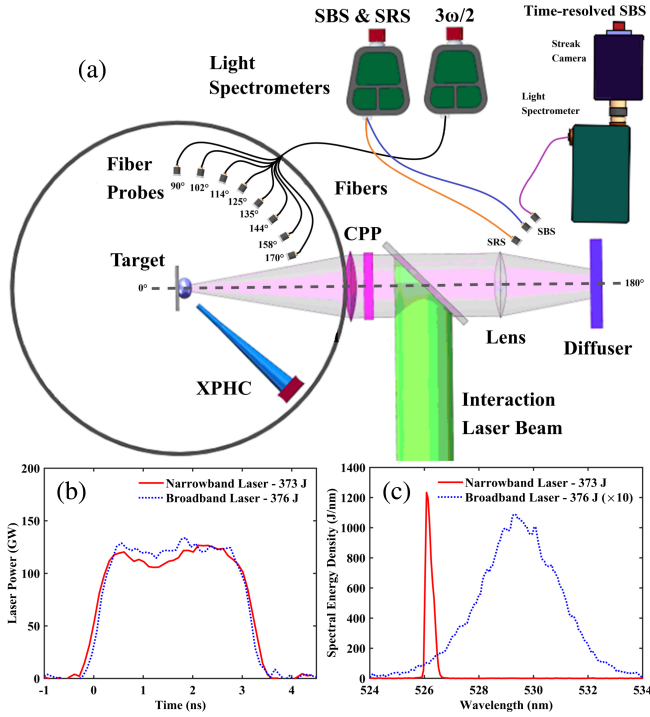
FIG. 1. (a) Schematic diagram of the experimental setup. The labeled angles are scattering angles θ, where 0° refers to the laser incidence and 180° the backward direction. (b) Laser waveforms at energy (E_L) of ~375 J of narrow band and broadband lasers. (c) Laser spectra correspond to (b). The center wavelengths of narrow band and broadband lasers are, respectively, 526.1 and 529.3 nm, and the bandwidths are < 0.01 and 3.2 nm (full width at half maximum), so the relative bandwidths are < 0.01% and ~0.6%. Note the measured bandwidth of the narrow band laser is limited by the insufficient spectral resolution.

bandwidth (full width at half maximum) [35]. The relative bandwidth of the broadband laser is $\Delta\omega/\omega_0 \approx 0.6\%$, where $\Delta\omega$ and ω_0 are the bandwidth and center angular frequency, respectively. The coherence time of the broadband laser is $\tau_c \approx 2/\Delta\omega \approx 0.1$ ps, as its spectrum approximately fits a Lorentzian function [12]. Both the lasers have an f number of 4.2, and they are applied with a continuous phase plate (CPP) to form relatively uniform irradiance.

The experimental setup is schematically illustrated in Fig. 1(a), and typical laser waveforms and spectra are sequentially presented in Figs. 1(b) and 1(c). 100–400-J (E_L), ~3.2-ns square laser pulses (narrow band and broadband) irradiated normally at 30-μm-thick planar parylene-n (C_8H_8) targets with 15-μm-thick titanium layer on the back. The laser spot size is approximately 180 μm, resulting in average laser intensities (I_L) of 1.2–4.9×10^{14} W/cm². Time-integrated SBS and SRS backscatters within the full aperture of the final optics were collected by fiber probes facing a wavelength-insensitive diffuser at the laser backward, which were further measured by a multichannel light spectrometer using a 50-grooves/mm grating with a spectral resolution of 1.7 nm. The responsivity of the

above diagnostic was calibrated using a standard light source with a known power spectrum, which was placed at the target chamber center facing the laser backward and the light within the focusing cone was collected, whose gross power spectrum was calculated by integration over solid angle. The responsivity was then obtained by comparing the output and input spectra, where the output is the measured spectrum and the input is the gross energy spectrum calculated by multiplying the gross power spectrum by exposure time. Several sets of responsivity were obtained with different exposure times, and the arithmetic mean was used as the average responsivity while the root-mean-square deviation corresponded to the errors.

As the above diagnostic covers the broad wavelength produced by SRS, the spectral resolution for the SBS backscatter is insufficient. More precise time-resolved spectra of the SBS backscatter were obtained by a streak camera connected to a high-resolution spectrometer using a 1200-grooves/mm grating with a spectral resolution of 0.1 nm. Time-integrated three-halves harmonic emission ($3\omega/2$) at various scattering angles (θ) were collected by another multichannel spectrometer using a 2400-grooves/mm grating with a spectral resolution of 0.05 nm. The number of valid shots for each spectral diagnostic is not identical, as the diagnostics were added to the experiments gradually. Laser spots were imaged by an x-ray pinhole camera (XPHC), which measured the soft x-ray self-luminescence of the targets.

Figure 2(a) presents the measured spectra of the SBS backscatter at roughly ~100, ~200, ~300, and ~400 J, in which the spectral shapes were blurred by the limited resolution. Nevertheless, the results are still useful for the comparison of scattering energy based on the intensity-energy calibration, which is shown in Fig. 2(b). The variation of the SBS backscatter energy within the full aperture of the final optics ($E_{s,SBS}$) is almost linear to the laser incident energy in both the narrow band and broadband cases, resulting in fairly stable scattering rates of ~4% for the narrow band laser and ~2% for the broadband laser, indicating that the SBS backscattering was robustly reduced by half with the 0.6% bandwidth. Note these low backscattering levels are responsible for the scatters within the small solid angle (0.036 sr) occupied by the focusing cone. In plasmas produced by laser irradiating solid targets, the energy scattered at angles larger than the focusing cone can be similar or even higher than that backscattered in the cone [1].

Figures 2(c) and 2(d) are sequentially the time-resolved SBS spectra with the narrow band and broadband lasers at ~375 J obtained by the streak camera. With higher resolution, a two-peak structure is found in the spectrum under the narrow band condition, which is not seen in the broadband case owing to the wide laser spectrum. A possible interpretation of the two peaks is that the redshift peak might be associated with the nonlinear SBS in the
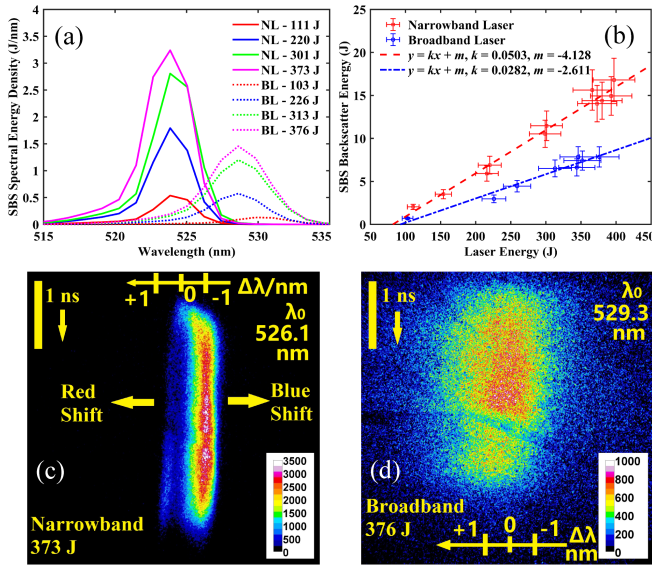
FIG. 2. Experimental results regarding the SBS backscatter. (a) Measured time-integrated spectra at roughly $\sim$100, $\sim$200, $\sim$300, $\sim$400 J. Here "NL" and "BL" refer to the narrow band and broadband lasers, respectively [same in Figs. 3(a) and 4(a)]. (b) $E_{\mathrm{s,SBS}}$ within the full aperture of the final optics versus incident energy, based on the time-integrated spectra. The dashed curves are linear fittings for the measured data points. (c) Time-resolved spectra with the narrow band laser at $\sim$375 J obtained by the streak camera. (d) Time-resolved spectra with the broadband laser at $\sim$375 J. Note the dark bands with sharp edges at the central part of the signals in (c) and (d) are induced by the unevenness response of the steak camera rather than a physical phenomenon.

dense plasma near the critical surface [36] or the reflection of laser light at the critical density while the blueshift peak is possibly due to the SBS stimulated in a region moving away for the target (Doppler effect) [37]. In the broadband case, the spectrum presents a small redshift increasing with time, which is different from the narrow band case.

The time-integrated spectra and the full aperture energy of the SRS backscatters are shown in Figs. 3(a) and 3(b), respectively. The spectral difference between narrow band and broadband cases suggests that SRS in the two cases occurred mainly in different plasma regions. Specifically, SRS is more likely to occur in relatively higher-density regions under broadband conditions, and the reason may be related to the mitigation of laser filamentation by the bandwidth [38], as filament formed in an underdense region could enhance the localized light intensity and make the spectrum present peaks at shorter wavelengths. Figure 3(b) suggests an exponential relation between the SRS backscatter energy ($E_{\mathrm{s,SRS}}$) and E_{L}, which is different from the linear relation for SBS. As the exponential factor b of the fitting curve in the broadband case is larger, the reduction of SRS is significant at low laser energy but gradually fades with more intense lasers. Thus, one may expect a loss of effectiveness of the bandwidth at a certain
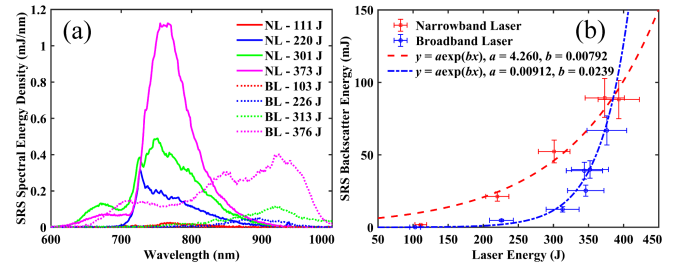

FIG. 3. Experimental results regarding the SRS backscatter. (a) Measured time-integrated spectra at roughly $\sim$100, $\sim$200, $\sim$300, $\sim$400 J. (b) $E_{\mathrm{s,SRS}}$ within the full aperture of the final optics versus incident energy, based on the time-integrated spectra. The dashed curves are exponential fittings for the measured data points.

energy higher than those of the experiments. Besides, $E_{\mathrm{s,SRS}}$ is 2 orders of magnitude weaker than $E_{\mathrm{s,SBS}}$, indicating SBS is the main energy-loss mechanism under such conditions.

Figure 4(a) shows the average spectra of $3\omega/2$ over various scattering angles to represent the overall situation of LPI at quarter-critical density, while the angular distribution here is not analyzed in detail. The two-peak structure in the narrow band case suggests that the spectra were mainly produced by TPD. The spectra in the broadband case only have one peak, which may be attributed to absolute SRS at quarter-critical density or the spectral mixing of two-peak spectra produced by different frequency components within the bandwidth. Figure 4(b) shows the relations between the average $3\omega/2$ integrated intensity and E_{L} under the narrow band and broadband conditions. As $3\omega/2$ is not a direct measurement of TPD or absolute SRS, the reduction may suggest a weaker LPI at quarter-critical density, which should be investigated more precisely in the future with dedicated measurements and simulations.

The incident energy of 375 J is discussed as an example for further theoretical calculations, which corresponds to
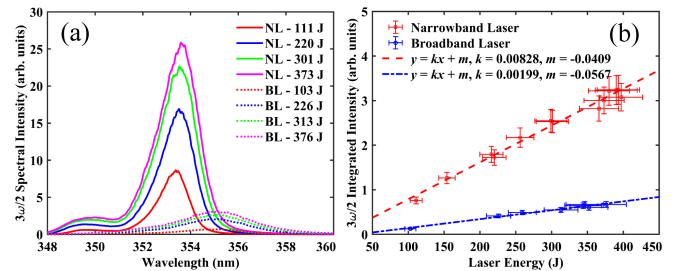

FIG. 4. Experimental results regarding $3\omega/2$. (a) Measured time-integrated spectra at roughly $\sim$100, $\sim$200, $\sim$300, and $\sim$400 J. The curves refer to average spectra over different scattering angles. (b) Average $3\omega/2$ integrated intensity over different scattering angles versus incident energy, based on the time-integrated spectra. The dashed curves are linear fittings for the measured data points.

the laser intensity of 4.6×10^{14} W/cm^2. Radiation hydrodynamics (RHD) simulations have been performed to estimate the plasma conditions by use of the FLASH code [39,40]. With experimental laser conditions and a flux limiter of 0.06 for CH plasmas, a density scale length (L) of ~ 170 μm, an electron temperature of ~ 1 keV, and an ion temperature of ~ 0.5 keV were obtained. The temperature given by the simulations suggests that the SRS cutoff at low densities with the narrow band laser shown in Fig. 3(a) was produced by Landau damping, which gives a value of ~ 0.9 keV [11,41].

For SBS backscattering, the linear growth rate with the bandwidth (γ_B) in homogeneous plasmas is estimated by $\gamma_B \Delta\omega / \gamma_0^2 \approx (k_s/k_0)^{-1} \arctan(4P/\gamma_B)(0.5\Delta\omega/P + 0.45P/\omega_0)$ [23], where $P \approx 1.1\Delta\omega(1 - n_e/n_{cr})^{1/2}$, $\gamma_0/\omega_0 \approx 3.4 \times 10^{-2} I_{14}^{1/2} \lambda_\mu \{(1 - k_s^2/k_0^2)(n_e/n_{cr})(1 - n_e/n_{cr})[Z/(ZT_{e,keV} + 3T_{i,keV})]\}^{1/2}$ is the normalized monochromatic growth rate [11], n_e and n_{cr} are, respectively, the local electron density and the critical density corresponding to the laser wavelength, k_s and k_0 are the wave numbers of the scattered and incident light, respectively, $Z \approx 3.5$ is the average ionization of CH plasma, I_{14} is the laser intensity in 10^{14} W/cm^2, $\lambda_\mu \approx 0.53$ is the laser wavelength in microns, and $T_{e,keV}$ and $T_{i,keV}$ are the electron and ion temperatures in kilo-electron volts, respectively. For a given n_e/n_{cr}, k_s/k_0 can be calculated based on the matching conditions and the simulated plasma parameters, which further gives γ_0 and γ_B. One obtains $\gamma_0/\omega_0 \lesssim 1.2 \times 10^{-3}$ and $\gamma_0/\gamma_B \sim 10$ for $n_e/n_{cr} = 0.01$–0.99, implying a solid mitigation effect of the bandwidth on the local growth of SBS within a wide range of densities. Considering γ_0 only, one has $\Delta\omega/\gamma_0 \gtrsim 5$, which makes the reduction of growth rate accessible even based on a concise estimation of $\gamma_B \sim \gamma_0^2/\Delta\omega$.

The above discussion demonstrates that the growth rate of SBS is decreased by the broadband laser. The subsequent convective amplification of scattering light during the propagation in large-scale inhomogeneous plasmas can also be mitigated by the reduction of driven force and the weak coupling of frequencies [42]. Considering the scale length of fluid velocity, the 0.6% bandwidth is sufficient to mitigate the SBS reflectivity [9]. Similar to the CBET process [32], a bandwidth larger than $3\omega_{iaw}$ may effectively suppress the convective amplification of SBS. Here, $\omega_{iaw} = k_i c_s \approx 2\omega_0(c_s/c)(1 - n_e/n_{cr})^{1/2} < 1.8 \times 10^{-3}\omega_0$, when $k_i \approx 2k_0$, in which ω_{iaw} and k_i are, respectively, the frequency and wave number of the ion acoustic wave, and $c_s \approx 0.9 \times 10^{-3}c$ is the ion-sound velocity for the simulated plasma parameters. As $3\omega_{iaw}/\omega_0 < 0.6\%$, the convective amplification of SBS could be mitigated by the bandwidth. Therefore, the reduction of SBS reflectivity in the experiments was attributed to the bandwidth by reducing the growth rate and convective amplification.

Figure 5 shows the two-dimensional particle-in-cell (PIC) simulation results performed by the OSIRIS code
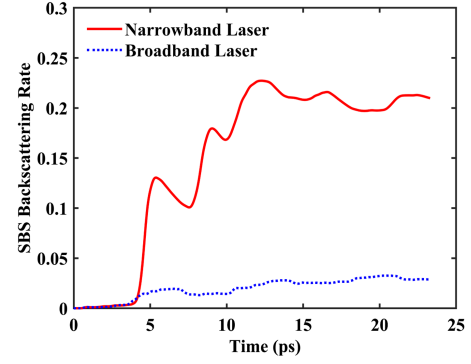

FIG. 5. The two-dimensional PIC simulation results of the SBS backscattering rates with the narrow band and broadband lasers. The plasma conditions are $T_e = 1$ keV, $T_i = 0.5$ keV, and $L = 170$ μm, while the laser intensity is 4.6×10^{14} W/cm^2 corresponding to 375 J energy. The simulations last for 23.3 ps, and the plasmas cover a density range of 0.07–$0.8 n_{cr}$. The longitudinal and transverse sizes of the simulation box are 500 and 50 μm, respectively.

[43] regarding the SBS backscattering rates with the narrow band and broadband lasers. A significant reduction of SBS by the broadband laser is found at $t = 5$ ps, which is saturated after $t = 12$ ps. The simulation results are qualitatively consistent with the experiments and support the analyses of the direct reduction of the growth and saturation level by the bandwidth. Although the absolute value of scattering rate given by PIC simulation is usually not so accurate for its 2 orders of magnitude shorter pulse duration compared to the ns laser, it can still qualitatively reflect the characteristics of the related physics—the 0.6% bandwidth can robustly mitigate the SBS backscattering.

For SRS backscattering, γ_B is calculated by $\gamma_B \Delta\omega / \gamma_0^2 = 4/[1 + (k_s/k_0)(\lambda_s/\lambda_0)]$ [26], where $\gamma_0/\omega_0 \approx 2.1 \times 10^{-3} I_{14}^{1/2} \lambda_\mu (1 + k_s/k_0)[(n_e/n_{cr})(1 - n_e/n_{cr})]^{1/2}[(\lambda_0/\lambda_s)(1 - \lambda_0/\lambda_s)]^{-1/2}$ [11], and λ_s is the scattering wavelength. Let $\lambda_s = 800$ nm be an example, one has $n_e/n_{cr} \approx 0.1$ and $k_s/k_0 \approx 0.6$ according to the dispersion relations and matching conditions for SRS when $T_e = 1$ keV, which gives $\gamma_0/\omega_0 \approx 2.5 \times 10^{-3}$ and $\gamma_B/\omega_0 \approx 2.2 \times 10^{-3}$. The calculated growth rates indicate the temporal growth of SRS is slightly reduced by the bandwidth, but the reduction is much less than that of SBS. For spatial growth, the extension of the interaction length can compensate for the reduction of local growth rate [26].

Although the 0.6% bandwidth may not be sufficient to reduce SRS directly, it may still affect instabilities by the mitigation of filamentation for the positive dependence of the growth rates to the light intensity. The required bandwidth for mitigating filaments induced by the ponderomotive force and thermal effects is estimated by $\Delta\omega/\omega_0 > 5.1 \times 10^{-3}(I_{14}/T_{e,keV})(n_e/n_{cr})\lambda_\mu^2 H$ [44], where $H \sim 2$ is a factor to account for thermal effects. Substituting $n_e/n_{cr} \leq 1/4$ for SRS into the above inequality, one has

$\Delta\omega/\omega_0 > 0.3\%$, which is satisfied in the experiments. Thus, the observed reduction of SRS backscattering may be mainly attributed to the mitigation of filaments rather than a direct suppression by the bandwidth. For comparison, the required bandwidth for mitigating SBS and CBET is $\Delta\omega/\omega_0 \gtrsim 3\omega_{\mathrm{iaw}}/\omega_0 \sim 0.3\%$ when $c_s/c \sim 10^{-3}$ and $n_e/n_{\mathrm{cr}} \sim 3/4$, which is similar to that for mitigating filamentation in underdense plasmas.

A bandwidth of 0.3% was used to investigate the behavior of SRS in Ref. [45], where the SRS reflectivity with the broadband laser was reduced in the solid target configuration, and the fitting curves were close to the exponential dependence when $I < 5 \times 10^{14}$ W/cm^2. The above results are similar to ours, except for the SRS reflectivity per solid angle [J/(J · sr)] at $\sim 5 \times 10^{14}$ W/cm^2 in that work was $\sim 10^{-2}$ with the narrow band laser and $\sim 10^{-6}$ with the broadband laser, while the values of ours are sequentially 7×10^{-3} and 5×10^{-3}. Their larger former value (10^{-2}) could be attributed to the larger ~ 260 μm scale length, and their much smaller latter value (10^{-6}) may be explained by the spatial incoherence induced by the fiber optics they used, suggesting that SRS could be further reduced by spatial incoherence in addition to temporal incoherence, which is consistent to the observation in Ref. [46] that the SRS backscatter was reduced by more than two orders of magnitude at $\sim 5 \times 10^{14}$ W/cm^2 with induced spatial incoherence (ISI). Nevertheless, the reason for SRS reduction could be attributed to the improvement of irradiance homogeneity induced by the mitigation of filamentation or other beam-smoothing techniques [47].

In summary, our experimental results confirm that a 0.6% bandwidth could lead to a certain amount of reduction of the scatters produced by various laser-plasma instabilities, where the effect on the SBS backscattering is robust, but the effect on the SRS backscattering is not. This suggests that broadband lasers may have a significant effect on improving laser absorption, since SBS (CBET in the multibeam configuration) is the main cause of laser energy loss especially under the direct-drive scheme. The different reasons for the reductions of the scatters reveal the necessity for continuous development of large-bandwidth low-coherence laser technology, until direct suppression of major LPI is achieved in DDICF.

A. L. and N. K. contributed equally to this work.

*lal@siom.ac.cn
†kangning@siom.ac.cn
‡zhaoyao5@mail.sysu.edu.cn

[1] R. S. Craxton *et al.*, Phys. Plasmas **22**, 110501 (2015).
[2] E. M. Campbell *et al.*, Phil. Trans. R. Soc. A **379**, 20200011 (2020).
[3] O. A. Hurricane, P. K. Patel, R. Betti, D. H. Froula, S. P. Regan, S. A. Slutz, M. R. Gomez, and M. A. Sweeney, Rev. Mod. Phys. **95**, 025005 (2023).
[4] T. J. Kessler, Y. Lin, J. J. Armstrong, and B. Velazquez, Proc. SPIE Int. Soc. Opt. Eng. **1870**, 95 (1993).
[5] S. Skupsky, R. W. Short, T. Kessler, R. S. Craxton, S. Letzring, and J. M. Soures, J. Appl. Phys. **66**, 3456 (1989).
[6] T. R. Boehly, V. A. Smalyuk, D. D. Meyerhofer, J. P. Knauer, D. K. Bradley, R. S. Craxton, M. J. Guardalben, S. Skupsky, and T. J. Kessler, J. Appl. Phys. **85**, 3444 (1999).
[7] Y. Q. Gao *et al.*, Matter Radiat. Extremes **5**, 065201 (2020).
[8] H. H. Ma, X. F. Li, S. M. Weng, S. H. Yew, S. Kawata, P. Gibbon, Z. M. Sheng, and J. Zhang, Matter Radiat. Extremes **6**, 055902 (2021).
[9] Y. Zhao, Z. M. Sheng, Z. J. Cui, L. Ren, and J. Q. Zhu, New J. Phys. **24**, 043025 (2022).
[10] J. J. Thomson and J. I. Karush, Phys. Fluids **17**, 1608 (1974).
[11] W. Kruer, *The Physics of Laser Plasma Interactions* (CRC Press, Boca Raton, 2003).
[12] R. K. Follett, J. G. Shaw, J. F. Myatt, C. Dorrer, D. H. Froula, and J. P. Palastro, Phys. Plasmas **26**, 062111 (2019).
[13] G. Laval, R. Pellat, D. Pesme, A. Ramani, Marshall N. Rosenbluth, and E. A. Williams, Phys. Fluids **20**, 2049 (1977).
[14] L. Lu, Phys. Fluids **31**, 3362 (1988).
[15] L. Lu, Phys. Fluids B **1**, 1605 (1989).
[16] L. Divol, Phys. Rev. Lett. **99**, 155003 (2007).
[17] P. N. Guzdar, W. Tan, Y. C. Lee, C. S. Liu, and R. H. Lehmberg, Phys. Fluids B **3**, 776 (1991).
[18] Y. Zhao, S. M. Weng, Z. M. Sheng, and J. Q. Zhu, Plasma Phys. Controlled Fusion **61**, 115008 (2019).
[19] Y. Zhao, C. F. Wu, S. M. Weng, Z. M. Sheng, and J. Q. Zhu, Plasma Phys. Controlled Fusion **63**, 055006 (2021).
[20] K. Estabrook and W. L. Kruer, Phys. Fluids **26**, 1892 (1983).
[21] Y. Zhao, S. M. Weng, M. Chen, J. Zheng, H. B. Zhuo, and Z. M. Sheng, Matter Radiat. Extremes **2**, 190 (2017).
[22] J. E. Santos, L. O. Silva, and R. Bingham, Phys. Rev. Lett. **98**, 235001 (2007).
[23] B. Brandao, J. E. Santos, R. M. G. M. Trines, R. Bingham, and L. O. Silva, Plasma Phys. Controlled Fusion **63**, 094003 (2021).
[24] K. Estabrook, W. L. Kruer, and B. F. Lasinski, Phys. Rev. Lett. **45**, 1399 (1980).
[25] G. Bonnaud and C. Reisse, Nucl. Fusion **26**, 633 (1986).
[26] P. N. Guzdar, C. S. Liu, and R. H. Lehmberg, Phys. Fluids B **3**, 2882 (1991).
[27] D. F. DuBois, B. Bezzerides, and H. A. Rose, Phys. Fluids B **4**, 241 (1992).

[28] R. K. Follett, J. G. Shaw, J. F. Myatt, J. P. Palastro, R. W. Short, and D. H. Froula, Phys. Rev. Lett. **120**, 135005 (2018).

[29] J. W. Bates, J. F. Myatt, J. G. Shaw, R. K. Follett, J. L. Weaver, R. H. Lehmberg, and S. P. Obenschain, Phys. Rev. E **97**, 061202(R) (2018).

[30] J. A. Marozas *et al.*, Phys. Rev. Lett. **120**, 085001 (2018).

[31] J. W. Bates, R. K. Follett, J. G. Shaw, S. P. Obenschain, R. H. Lehmberg, J. F. Myatt, J. L. Weaver, D. M. Kehne, M. F. Wolford, M. C. Myers, and T. J. Kessler, High Energy Density Phys. **36**, 100772 (2020).

[32] A. G. Seaton, L. Yin, R. K. Follett, B. J. Albright, and A. Le, Phys. Plasmas **29**, 042707 (2022).

[33] Y. Q. Gao *et al.*, Opt. Lett. **45**, 6839 (2020).

[34] Y. Cui, Y. Gao, D. Rao, D. Liu, F. Li, L. Ji, H. Shi, J. Liu, X. Zhao, W. Feng, L. Xia, J. Liu, X. Li, T. Wang, W. Ma, and Z. Sui, Opt. Lett. **44**, 2859 (2019).

[35] L. Ji, X. Zhao, D. Liu, Y. Gao, Y. Cui, D. Rao, W. Feng, F. Li, H. Shi, J. Liu, X. Li, L. Xia, T. Wang, J. Liu, P. Du, X. Sun, W. Ma, Z. Sui, and X. Chen, Opt. Lett. **44**, 4359 (2019).

[36] A. V. Maximov, J. Myatt, W. Seka, R. W. Short, and R. S. Craxton, Phys. Plasmas **11**, 2994 (2004).

[37] J. Myatt, A. V. Maximov, W. Seka, R. S. Craxton, and R. W. Short, Phys. Plasmas **11**, 3394 (2004).

[38] S. P. Obenschain, C. J. Pawley, A. N. Mostovych, J. A. Stamper, J. H. Gardner, A. J. Schmitt, and S. E. Bodner, Phys. Rev. Lett. **62**, 768 (1989).

[39] B. Fryxell, K. Olson, P. Ricker, F. X. Timmes, M. Zingale, D. Q. Lamb, P. MacNeice, R. Rosner, J. W. Truran, and H. Tufo, Astrophys. J. Suppl. Ser. **131**, 273 (2000).

[40] A. Dubey, K. Antypas, M. K. Ganapathy, L. B. Reid, K. Riley, D. Sheeler, A. Siegel, and K. Weide, Parallel Comput. **35**, 512 (2009).

[41] N. Kang, H. Y. Liu, Y. Zhao, S. Z. Ji, S. L. Zhou, and A. L. Lei, Plasma Phys. Controlled Fusion **62**, 055007 (2020).

[42] Y. Zhao, H. Yin, B. Zhao, and Z. Cui, Nucl. Fusion **64**, 016022 (2024).

[43] R. A. Fonseca, L. O. Silva, F. S. Tsung, V. K. Decyk, W. Lu, C. Ren, W. B. Mori, S. Deng, S. Lee, T. Katsouleas, and J. C. Adam, *Computational Science ICCS 2002* (Springer, Berlin, Heidelberg, 2002), Vol. 2331, p. 342, 10.1007/3-540-47789-6_36.

[44] D. S. Montgomery, J. D. Moody, H. A. Baldis, B. B. Afeyan, R. L. Berger, K. G. Estabrook, B. F. Lasinski, E. A. Williams, and C. Labaune, Phys. Plasmas **3**, 1728 (1996).

[45] C. Rousseaux, B. Meyer, and G. Thiell, Phys. Plasmas **2**, 2075 (1995).

[46] S. E. Coe, T. Afshar-Rad, M. Desselberger, F. Khattak, O. Willi, A. Giulietti, Z. Q. Lin, W. Yu, and C. Danson, Europhys. Lett. **10**, 31 (1989).

[47] N. Kang, H. Liu, S. Zhou, Y. Zhao, and A. Lei, J. Opt. Soc. Am. B **38**, 3567 (2021).